Cross sections for (n, xn) reactions between 7.5 and 28 MeV

B. P. Bayhurst, J. S. Gilmore, R. J. Prestwood, J. B. Wilhelmy, Nelson Jarmie, B. H. Erkkila, and R. A. Hardekopf
University of California, Los Alamos Scientific Laboratory, Los Alamos, New Mexico 87544
(Received 16 April 1975)

A total of 236 cross sections for (n,xn) reactions have been measured at neutron energies between 7.5 and 28 MeV, using radiochemical techniques. Cross sections for (n,n') and $(n,2n)$ reactions are reported on ^{193}Ir; $(n,2n)$ cross sections on ^{45}Sc and ^{58}Ni; $(n,2n)$ and $(n,3n)$ cross sections on ^{89}Y, ^{90}Zr, and ^{107}Ag; $(n,2n)$, $(n,3n)$, and $(n,4n)$ cross sections on ^{169}Tm, ^{175}Lu, ^{191}Ir, ^{197}Au, and ^{203}Tl; $(n,3n)$ and $(n,4n)$ cross sections on ^{151}Eu; and $(n,4n)$ cross sections on ^{205}Tl. Neutron fluences were determined by either the ^{27}Al$(n,\alpha)^{24}$Na or the ^{90}Zr$(n,2n)^{89}$Zr reactions appropriately combined with proton-recoil telescope measurements. The excitation functions are compared with calculations based on a model incorporating both compound-nucleus and preequilibrium decay modes. Cross sections for the ^{27}Al$(n,\alpha)^{24}$Na reaction between 21 and 26 MeV are also reported.

NUCLEAR REACTIONS ^{27}Al(n,α), $E=21.4$–26.0 MeV; ^{45}Sc$(n,2n)$, $E=14.1$–28.1 MeV; ^{58}Ni$(n,2n)$, $E=16.2$–28.1 MeV; ^{89}Y$(n,2n)$, $(n,3n)$, $E=14.1$–28.1 MeV; ^{107}Ag$(n,2n)$, $(n,3n)$, $E=13.4$–28.1 MeV; ^{151}Eu$(n,3n)$, $(n,4n)$, $E=14.8$–28.0 MeV; ^{169}Tm$(n,2n)$, $(n,3n)$, $(n,4n)$, $E=8.6$–28.0 MeV; ^{191}Ir$(n,2n)$, $E=8.6$–24.5 MeV; ^{191}Ir$(n,3n)$, $(n,4n)$, $E=16.2$–28.0 MeV; ^{193}Ir(n,n), $E=7.6$–14.7 MeV; ^{193}Ir$(n,2n)$, $E=8.6$–21.2 MeV; ^{197}Au$(n,2n)$, $(n,3n)$, $(n,4n)$, $E=8.6$–28.1 MeV; ^{203}Tl$(n,2n)$, $(n,3n)$, $(n,4n)$, $E=8.6$–28.0 MeV; ^{205}Tl$(n,4n)$, $E=23.3$–28.0 MeV; Zr(n,xn), $E=14.1$–28.1 MeV; Lu(n,xn), $E=8.5$–28.0 MeV; measured $\sigma(E)$. Estimated ^{90}Zr$(n,2n)$, $(n,3n)$, ^{175}Lu$(n,2n)$, $(n,3n)$, $(n,4n)$, $\sigma(E)$. Comparison with combined statistical and preequilibrium model.

RADIOACTIVITY ^{189,190}Ir, ^{193}Ir^m; measured $T_{1/2}$.

I. INTRODUCTION

A number of authors[1-3] have interpreted the rising portion of $(n, 2n)$ excitation functions by the statistical model of nuclear reactions originally described by Weisskopf and collaborators.[4] Liskien expanded this concept to the successive emission of three neutrons and found good agreement between predictions and experimental $(n, 3n)$ cross sections of several nuclei of intermediate mass between 18.2 and 19.5 MeV.[5] Recently, several articles on nuclear reactions at moderate excitation energies have been concerned with the emission of particles before the nucleus reaches statistical equilibrium.[6-10] This paper reports experimental (n, xn) excitation functions for target nuclei ranging from mass 45 to 205 for neutron energies up to 28 MeV. In an attempt to understand the reaction mechanism, the data have been compared to a model which permits both preequilibrium and statistical modes of decay.

Threshold reactions including (n, n') and $(n, 2n)$ have been used extensively for determining the differential flux $d\phi/dE$ from neutron sources by foil activation techniques. The higher order (n, xn) reactions should aid in characterizing spallation neutron sources by extending the neutron-energy range for this type of dosimetry above 20 MeV.

Cross section measurements by radiochemical techniques at neutron energies above 20 MeV present several difficulties which do not exist at 14 MeV. For one, the fluxes using gas-target sources are smaller and the types of reactions in the samples more numerous. Although the individual isotopes might have been more conveniently determined by means of the high resolution of semiconductor detectors, the low activities produced in the irradiations required the use of highly efficient NaI(Tl) scintillation detectors. Another difficulty which Henkel, Perry, and Smith,[11] Cranberg, Armstrong, and Henkel,[12] and Kuzmin *et al.*[13] have pointed out is that the ^{2}H-^{2}H and ^{2}H-^{3}H reactions are not sources of monoenergetic neutrons when deuterium breakup is energetically possible, and that other neutrons may come from reactions on the structural materials of the beam tube and target gas container itself. Since the breakup neutrons arise from a three-body system, they have a continuum of energies, of which only the upper limit can be calculated from the collision kinematics. Fortunately, the unwanted neutrons will not affect radiochemical measurements if they are below the thresholds of the reactions being studied.

TABLE I. Summary of the nominal neutron energy E_n, the source reaction, machine energy E_i of the incident charged particle, and fluence for the irradiations.

E_n (MeV)	Source reaction	E_i (MeV)	Fluence (10^{11} n/cm^2)	Fluence monitor	E_n(max) from ^{2}H breakup (MeV)	$\left(\frac{\text{Blank}}{\text{Live}}\right)_{\text{Al}(n,\alpha)}$	$\left(\frac{\text{Blank}}{\text{Live}}\right)_{\text{Au}(n,2n)}$	"Effective" Au(n,γ) cross section (b)
7.6	^{1}H$(t,n)^3$He	12.20	146	^{27}Al$(n,\alpha)^{24}$Na		0.074	1.01 ± 0.02 [a]	0.05
8.6	^{1}H$(t,n)^3$He	14.00	63	^{27}Al$(n,\alpha)^{24}$Na		0.055	0.22	0.08
9.3	^{1}H$(t,n)^3$He	15.00	35	^{27}Al$(n,\alpha)^{24}$Na		0.068	0.10	0.10
13.4 to 14.9	^{3}H$(d,n)^4$He	0.30	14	^{27}Al$(n,\alpha)^{24}$Na	b			c
14.7	^{3}H$(d,n)^4$He	0.30	100	^{27}Al$(n,\alpha)^{24}$Na	b			c
16.2	^{2}H$(d,n)^3$He	13.63	24	^{90}Zr$(n,2n)^{89}$Zr Telescope	10.2		0.16	0.76
17.2	^{3}H$(d,n)^4$He	2.47	6.0	^{27}Al$(n,\alpha)^{24}$Na	b			c
18.2	^{3}H$(d,n)^4$He	2.94	3.1	^{27}Al$(n,\alpha)^{24}$Na	b			c
20.0	^{3}H$(d,n)^4$He	4.16	3.3	^{27}Al$(n,\alpha)^{24}$Na	0.8			0.01
21.3	^{2}H$(t,n)^4$He	5.25	3.4	^{27}Al$(n,\alpha)^{24}$Na Telescope	b			0.08
22.0	^{3}H$(d,n)^4$He	5.77	8.2	^{27}Al$(n,\alpha)^{24}$Na Telescope	2.8	0.005	≥0.007	0.29
23.3	^{2}H$(t,n)^4$He	6.29	2.2	^{27}Al$(n,\alpha)^{24}$Na Telescope	1.8	0.16	0.11	0.12
24.5	^{2}H$(t,n)^4$He	7.49	4.9	^{27}Al$(n,\alpha)^{24}$Na Telescope	3.0	0.33	0.18	0.54
26.0	^{2}H$(t,n)^4$He	8.98	3.5	Telescope	4.4	0.72	0.54	1.32
28.0	^{2}H$(t,n)^4$He	10.98	5.0	^{90}Zr$(n,2n)^{89}$Zr Telescope	6.1		0.31	1.93

[a] All neutrons above Au$(n,2n)$ threshold were produced from (t,n) reactions in beam stop.
[b] Incident particle is below threshold for deuterium breakup.
[c] ^{198}Au not detected.

II. EXPERIMENTAL

A. Irradiations

Table I summarizes the nominal neutron energy E_n (column 1), the source reaction, the machine energy E_i of the incident charged particle (column 3), and the fluence for the irradiations. Neutron energies between 13.4 and 14.9 MeV were obtained at the Los Alamos Cockcroft-Walton facility by using the variation of energy with laboratory angle of the $^3H(d, n)^4He$ reaction. The experimental arrangements have been described previously.[14,15] It suffices for this discussion to say that irradiations were made at the 15, 90, and 150° positions with respect to the direction of the deuteron beam using an air-cooled target and in the forward direction using a water-cooled target.

The remaining irradiations were made at the Los Alamos Van de Graaff facility.[15] Foil stacks consisting of alternate monitor and sample foils were held in a lightweight stainless steel holder at a carefully measured distance from the end of the 3-cm-long gas-target container. Distances between 10 and 15 mm were chosen to give both reasonable neutron-energy definition and sufficient foil activation. The charged-particle beam energy had an uncertainty of 10 keV. Integrated beam current and target gas pressure were recorded during the runs for decay corrections.

The $^{27}Al(n, \alpha)^{24}Na$ or $^{90}Zr(n, 2n)^{89}Zr$ reactions, or a proton-recoil telescope were used to measure fluences. Column 5 of Table I lists the fluence monitor reaction. For those energies at which this cross section was unknown, foils were also placed 80 and 90 mm behind the face of the foil stacks and on the face of a proton-recoil telescope to determine the monitor cross section in good geometry.

Column 6 of Table I lists the maximum energy of the neutrons produced by deuteron breakup in the gas for those irradiations in which deuterium was either the incident particle or the target. Since these secondary neutrons in the 16.2- and 28-MeV irradiations were above the 4.9-MeV effective threshold of our prime monitor reaction, $^{27}Al(n, \alpha)^{24}Na$, the $^{90}Zr(n, 2n)^{89}Zr$ reaction was used. For the 16.2-MeV irradiation, the breakup neutrons also extended above the thresholds of several of the $(n, 2n)$ products ($\geq$ 7.76 MeV), but they did not appear to produce enough activity to affect our cross section values at that energy.

The incident charged-particle energies were too low to produce triton-breakup neutrons in the gas in any of the irradiations. The thresholds for the $^1H(t, nd)^1H$, $^3H(d, nd)^2H$, and $^2H(t, nd)^2H$ reactions are 25.0, 10.4, and 15.6 MeV, respectively.

The foils were frequently activated by contaminant neutrons produced by incident charged-particle breakup and by (d, n) or (t, n) reactions on the window, the gold apertures, and gold beam stop of the target assembly. The (d, n) and (t, n) reactions on gold are inhibited by the Coulomb barrier, but have Q values of +4.878 and +5.269 MeV; thus, the maximum neutron energy is the sum of the incident particle energy and the Q value with a small center-of-mass correction. The disintegration rates of the samples and monitor foils were corrected for these "blanks" by measuring the activities in a second set of foils from an evacuated target irradiation when the incident particle energy was greater than 5.5 MeV. Columns 7 and 8 of Table I show the fractions of the total activity due to these spurious neutrons for the $^{27}Al(n, \alpha)^{24}Na$ monitors and for $^{197}Au(n, 2n)^{196}Au$ as a typical low threshold $(n, 2n)$ reaction.

Low energy neutrons from all of these secondary reactions also produced (n, γ) activities in several of the foils, thereby making the treatment of the counting data more difficult. These (n, γ) reactions also precluded the measurement of $^{193}Ir(n, 2n)$ cross sections above 21 MeV, since ^{192}Ir was formed by both reactions. To indicate the severity of (n, γ) activities, column 9 of Table I lists an "effective" cross section for the $^{197}Au(n, \gamma)^{198}Au$ reaction. These values were calculated by dividing the conversion $^{198}Au/^{197}Au_0$ by the fluence of "good" neutrons. As might be expected, most of the (n, γ) activity was from low energy neutrons produced by deuteron breakup in the gas rather than from the reactions in the evacuated target run.

B. Samples

Circular foils 9.5 mm in diameter were punched from the following metal sheets: 0.13-mm-thick Al; 0.06-mm Ni; 0.13-mm Zr; 0.08-mm Ag; 0.05-mm Au; and 0.03-mm Tl. Aluminum of 99.999% purity was procured from Ventron Corporation, Alpha Products. Both natural-isotopic-composition thallium and 92.25% enriched ^{203}Tl were used in the 24-, 26-, and 28-MeV neutron irradiations. Scandium, yttrium, europium, thulium, and lutetium foils were punched from 0.5-mm polyethylene sheets containing approximately 50% by volume of the appropriate oxide. The purity of the europium and lutetium oxides (Michigan Chemical Co.) and the thulium oxide (American Potash and Chemical Corp., Rare Earth Division) was 99.9%. The only impurities detectable by spectrographic analysis, other than rare earths, were 0.01% calcium and 0.005% magnesium. The iridium foils were 99.9% pure K_2IrCl_6 (Fairmont Chemical Co.) in polyethylene. The total length of the foil stack was ap-

proximately 7 mm.

After irradiation, the scandium, nickel, yttrium, and zirconium samples were separated from their (n, α) and (n, p) products by appropriate chemical steps before counting.[16] The three rare earth samples were ignited to remove the polyethylene binder. These samples were too heavy (approximately 100 mg) for the usual column separations; γ-ray pulse analysis and decay, however, failed to show any activities from impurities. The silver, iridium, gold, and thallium samples were purified by procedures similar to those by Kleinberg *et al.*[17]

C. Counting

(1) Aluminum, nickel, and scandium. The decay of ^{24}Na in the aluminum foils and the positron emitters ^{57}Ni and ^{44}Sc (in equilibrium with its ^{44}Sc^{m} parent) were followed on β proportional counters and the data treated by least-squares analysis.

(2) Yttrium. ^{88}Y was measured by integrating the 1.836-MeV photopeak from spectra recorded on a multichannel analyzer using a 76.2- by 76.2-mm external NaI(Tl) detector. ^{87}Y was determined from the 0.388-MeV photopeak of ^{87}Sr which had been chemically separated from its yttrium parent.

(3) Zirconium. ^{89}Zr was counted on a β proportional counter. After the ^{89}Zr had decayed, ^{88}Zr was measured by γ spectrometry using a 76.2- by 76.2-mm NaI(Tl) detector.

(4) Europium, thulium, and lutetium. The three rare earth samples were counted in a 76.2- by 76.2-mm NaI(Tl) well detector and associated multichannel analyzer and the various isotopes in the spectra resolved by a subtractive method. In this method for europium, for example, the ^{148}Eu counting rate was first determined from a high energy region of the spectrum. ^{149}Eu was then calculated from that part of the spectrum below 115 keV by subtracting the contribution of ^{148}Eu using a previously determined coefficient relating counting rates for the latter isotope in the high and low energy spectral regions. Small corrections determined by counting at late times were also applied in some of the irradiations for ^{150,152,154}Eu.

Similarly, a subtractive technique was used to determine ^{166}Tm, ^{167}Tm, and ^{168}Tm from the thulium spectra, and ^{172}Lu, ^{173}Lu, ^{174}Lu, and ^{177}Lu from the lutetium spectra. The contributions of the naturally occurring radioactive isotope ^{176}Lu, which were a major part of the total lutetium counting rate (30–65%), were calculated from the weight of the sample.

The coefficients used in the subtractive method and all of the necessary self-absorption corrections were determined on samples of the individual isotopes prepared by mass separation of materials irradiated at the Los Alamos cyclotron.

(5) Iridium. Spectra from a 127- by 127-mm NaI(Tl) well detector, and from a Reuter-Stokes Model No. RSG-61 Xe-CO_2 filled x-ray proportional counter were used to determine ^{188}Ir, ^{189}Ir, ^{190}Ir, ^{192}Ir, and ^{193}Ir^{m} using a subtractive method similar to that in Sec. IV. The samples of the individual isotopes used to measure half-lives, self-absorption corrections, and the coefficients for the subtractive method were prepared from irradiations at the Los Alamos cyclotron, Cockcroft-Walton, Omega West reactor, and critical assembly facilities with rhenium, natural Ir, or enriched ^{191}Ir and ^{193}Ir targets.

(6) Silver, gold, and thallium. The silver and gold samples were counted in 127- by 127-mm NaI(Tl) well spectrometers. Multicomponent least-squares analysis of the decay of selected energy regions of the spectra was used to resolve ^{105}Ag and ^{106}Ag^{m}, and ^{194}Au, ^{195}Au, ^{196}Au, and ^{198}Au. Similarly, ^{200}Tl, ^{201}Tl, and ^{202}Tl were resolved by decay using spectra from a 76.2- by 76.2-mm NaI(Tl) well spectrometer. Mass separated samples of these isotopes were used for the calibration experiments.

D. Absolute disintegration rates

The total detection efficiency for each isotope in a 127- by 127-mm NaI(Tl) well spectrometer was calculated using the curve of total efficiency as a function of photon energy calculated by the BURP computer program[18] and the decay schemes given in the Nuclear Data Sheets[19] or the Table of Isotopes.[20] The efficiency for our routine method of counting (β, integrated photopeak, or an energy region of a spectrum) was then measured relative to the well spectrometer efficiency by counting a sample of the individual isotope by both methods.

The total detection efficiencies from the BURP computer program have been experimentally verified at a number of photon energies by the sum coincidence method using radioisotopes with two or more photons in coincidence,[21] and by measuring the total-to-photopeak ratio for selected isotopes having a single photon.

For nuclides having complex decay schemes, the calculation of the disintegration rate from the total detection efficiency in a well counter rather than from the efficiency for a single photopeak has the advantage of being less sensitive to uncertainties in decay scheme details.

E. Proton-recoil telescope

For precise measurements where the cross section of a monitor radionuclide is not well known

TABLE II. $^{27}Al(n, \alpha)^{24}Na$ cross sections used in (n,xn) cross section calculations.

$\bar{E}_n$ (MeV)	$\Delta \bar{E}_n$ (MeV)	$^{27}Al(n, \alpha)^{24}Na$ σ(mb)
7.52		29.0
8.55		60.5
9.30		77.8
13.40		121
14.10		122
14.70		113
14.93		107
17.23		73.5
18.23		58.2
20.00		39.0
21.41	0.12	28.4± 1.4
22.18	0.09	24.7± 1.2
23.45	0.09	17.5± 0.9
24.58	0.07	15.0± 0.8
26.02	0.16	9.9± 0.5
Product $T_{1/2}$		15.00 h

(20–30 MeV), an alternate method for determining the neutron fluence was necessary. An accurate proton-recoil telescope has been developed[22] which will be described briefly. The telescope was similar to others[23] using a CH_2 radiator followed by two detectors in coincidence: a thin surface barrier silicon transmission detector and a NaI detector in which the recoil protons stopped. The detectors, separated by 13 cm, were supplied with apertures such that the stopping detector subtended only a 4° cone from the radiator. This tight geometry reduced the magnitude of the many geometric and kinematic corrections common to recoil telescopes. Low energy background neutrons from beam breakup and production from the target window and walls were discriminated by the energy measurement of the recoil protons in the NaI detector.

The resulting efficiency for neutron detection was low, about 2×10^{-5}. Coincidence rates for recoil protons were typically about 3 per sec, with singles rates in each detector about 1000 per sec.

The pulses from the detectors were processed with standard microsecond electronics and fed to an on-line computer (SDS-930) for convenient handling. An E-ΔE mass identification criteria, applied to the system because it was available, did not markedly improve the results, but it insured against spurious backgrounds.

The radiator-out background was very low; the error in the final fluence from this subtraction was less than 0.5%. When an evacuated target was used, no counts were seen. The only significant systematic *corrections* were those due to: finite geometry (1.0%), neutron absorption in the front wall of the telescope (1.1%), nuclear reactions in the NaI detector (0.6%), and dead time in the electronics (1.0%). The errors due to these corrections were negligible. Accidental coincidences were also negligible. The system was run long enough that the other error sources were larger than the statistical counting error (typically 0.5%). The final error of the neutron fluence determined by the telescope was 2 to 3%, dominated by the uncertainty in the $n+p$ differential cross section.[24]

The telescope, with a monitor foil on its face, was placed far enough back from the radiochemical foil stack so that the neutron flux was down to about 10^5 cm^{-2} sec^{-1}. In essence, the telescope was used to determine the absolute cross section of whatever monitor was placed on it; and other monitor foils of the same material interleaved in the foil stack determined the neutron fluences of the samples.

III. CALCULATIONS

The reaction cross sections were calculated from the disintegration rates of the sample and the average of the two adjacent monitor foils by the equation

$$\sigma_i = \left(\frac{D_i - RD_i'}{D_m - RD_m'}\right)\sigma_m \,, \tag{1}$$

where the subscripts i and m denote the unknown and monitor, respectively, and

$$D_i = \frac{(d/m)_i t}{N_i[1-\exp(-\lambda_i t)]} \,, \tag{2}$$

where d/m is the disintegration rate, corrected to the end of the irradiation, t is the length of the irradiation, λ is the decay constant, and N is the number of target atoms in the sample, calculated from the chemical composition, isotopic abundance, and weight of the sample. The prime denotes the same quantity determined from the evacuated target run, and R is the ratio of the integrated beam currents I/I' from the two runs.

The cross sections used for the $^{27}Al(n, \alpha)^{24}Na$ monitor reaction are given in Table II. Below 21 MeV they were derived from the compilation in Nuclear Data.[25] In estimating errors on the (n,xn) reaction cross sections, an absolute error (standard deviation) of 3% has been ascribed to these monitor cross sections. This uncertainty is considered realistic from various checks we have made such as intercomparison with the $^{115}In(n, n')^{115}In^m$ cross section as evaluated by Fabry *et al.*[26] (7–9 MeV), and determinations at the Los Alamos Cockcroft-Walton accelerator using fluences from

associated particle counting techniques (~14 MeV). The values for energies greater than 21 MeV are the ones determined using telescope fluences in these experiments. The cross sections for the $^{90}Zr(n, 2n)^{89}Zr$ monitors which were determined in the 16.2- and 28-MeV irradiations are in Table VI.

The relative fluence, the average energy $\bar{E}_n$, and the standard deviation $\Delta\bar{E}_n$ of the neutron-energy distribution incident at each foil position in an experiment were calculated by a simple Monte Carlo computer program (TIPI).[15] The finite source and foil geometry, the stopping power of the gas for the incident charged particle, and the cross section, differential yields, and kinematics of the source reaction were considered. Energy losses in the target window and gas were determined using stopping powers by Williamson, Boujot, and Picard.[27]

The constancy of the ratio of the fluence determined by the Al monitor foils to the relative fluence from the TIPI calculations (as a function of source distance) can be used to detect scattered or room return neutrons. In each irradiation except the 26 MeV, the ratio was constant within our experimental and computational errors. In that case, however, the ratio had increased by 10% by the back of the foil stack, and by 36% as the relative fluence decreased by a factor of 136. Since the effect of a more or less uniform scattered flux on the foils would be most evident where the high energy fluence was lowest, the aluminum cross section was determined from the foils nearest the gas target. All (n, xn) cross sections from the 26 MeV irradiation were calculated using the telescope fluence, and the *computed* relative fluence for the foils. Any effect of these lower energy neutrons on the $(n, 2n)$ cross section values at 26 and 28 MeV was not noticeable; nevertheless, extension of $(n, 2n)$ cross section determinations to higher energies would require auxiliary measurements of the fluence and spectrum of both scattered and breakup neutrons.

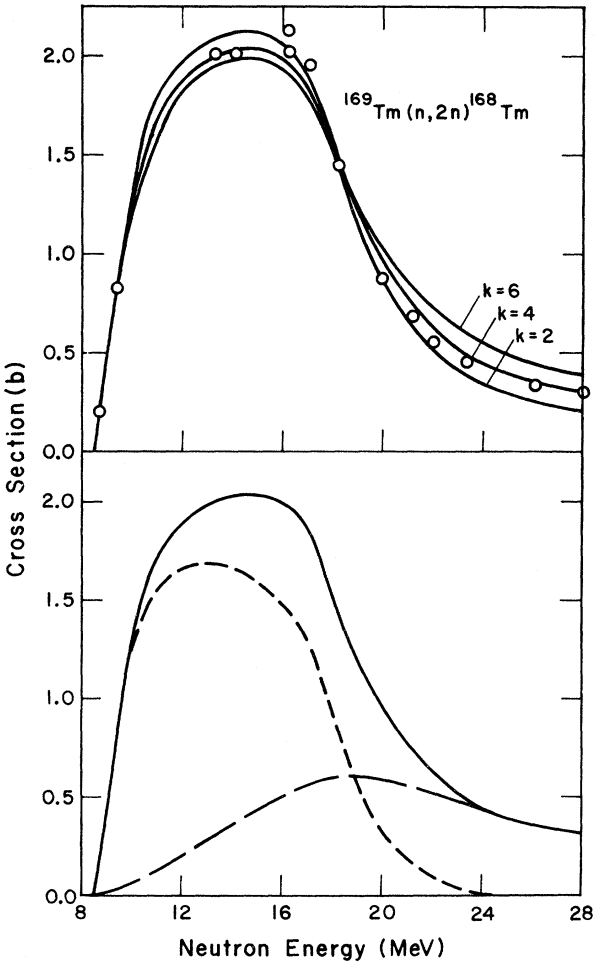

FIG. 1. Calculated and experimental cross sections for $^{169}Tm(n, 2n)^{168}Tm$. The upper half of the figure shows the fit of the calculations using three values of k, the scaling factor for the transition rate λ_{n+2} for internal transitions in the preequilibrium model. In the lower half, the solid curve represents the total $(n, 2n)$ cross section. The short-dashed curve shows the portion of the cross section due only to statistical deexcitation. The long-dashed curve represents the portion of the cross section which results from the preequilibrium emission of the first neutron.

IV. EXPERIMENTAL RESULTS

Tables III–XIV present the data for (n, xn) cross sections. The tables list the average neutron en-

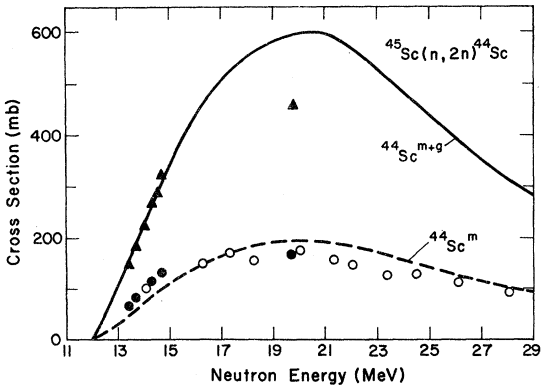

FIG. 2. Excitation function for $^{45}Sc(n, 2n)^{44}Sc$. Experimental cross sections for $^{45}Sc(n, 2n)^{44}Sc^{m}$ (○). The filled points are earlier measurements by Prestwood and Bayhurst (Ref. 14), normalized to the 14.1 MeV value of this work, for the isomeric (m) (●) and total (▲) cross sections. The lines are the results of calculations described in the text.

TABLE III. $^{45}Sc(n, 2n)^{44}Sc^m$ cross sections.

$\bar{E}_n$ (MeV)	$\Delta\bar{E}_n$ (MeV)	$^{45}Sc(n, 2n)^{44}Sc^m$ σ(mb)
14.10	0.05	105 ± 5
16.23	0.09	151 ± 8
17.25	0.16	169 ± 7
18.25	0.08	157 ± 8
20.01	0.09	174 ± 9
21.28	0.16	158 ± 7
22.04	0.11	147 ± 7
23.36	0.11	129 ± 6
24.50	0.11	130 ± 6
26.08	0.11	111 ± 4
28.06	0.13	92 ± 4
Product $T_{1/2}$		2.44 day
Threshold		11.57 MeV

TABLE IV. $^{58}Ni(n, 2n)^{57}Ni$ cross sections.

$\bar{E}_n$ (MeV)	$\Delta\bar{E}_n$ (MeV)	$^{58}Ni(n, 2n)^{57}Ni$ σ(mb)
16.21	0.11	63 ± 3
17.23	0.17	70 ± 5
18.24	0.09	76 ± 5
19.99	0.11	92 ± 6
21.26	0.18	93 ± 4
22.01	0.13	97 ± 4
23.36	0.11	102 ± 4
24.49	0.12	96 ± 4
26.06	0.12	87 ± 4
28.05	0.14	72 ± 3
Product $T_{1/2}$		36.0 h
Threshold		12.41 MeV

ergy $\bar{E}_n$ (column 1), the standard deviation of the neutron spectrum $\Delta\bar{E}_n$ (column 2), the cross sections and their uncertainties (one standard deviation) (column 3), plus the half-lives used in the calculations and the reaction thresholds. Cross section errors include errors due to counting and decay resolution, blank subtraction, weighing, the estimated systematic errors for absolute counting efficiencies, decay constants, and, for the monitor, cross section uncertainties. The data are also in Figs. 2–13 which will be discussed in Sec. VI. The plotted cross section uncertainties are the ones listed in the tables.

V. MODEL CALCULATIONS

The purpose of the model calculations was to give theoretical estimates of the total isotopic production cross sections for neutron-induced reactions in the 6- to 28-MeV energy range on a wide variety of target nuclei. The major emphasis is on (n, xn) reactions. We desired a model which would permit rapid computation over the broad energy range of the experimental data, have a minimum number of adjustable parameters, and would require little specific data on the nuclear properties of the individual isotopes.

The adopted model permits both statistical and preequilibrium deexcitation modes. The statistical portion uses standard evaporation theory which assumes the probability of emission of particles is proportional to their available phase space:

$$I(E_\beta) \propto g_\beta p_\beta{}^2 \sigma_{\text{inv}}(E_\beta)\rho(U - E_\beta - B_\beta)\ , \qquad (3)$$

where $I(E_\beta)$ is the intensity of the emitted particle β as a function of its energy E, g_β is the statistical weighting factor equal to $(2S_\beta + 1)$, p_β is the

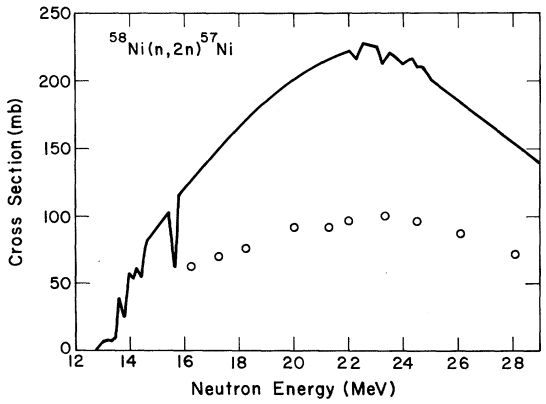

FIG. 3. Excitation function for $^{58}Ni(n, 2n)^{57}Ni$. Experimental cross sections (○) and calculated curve.

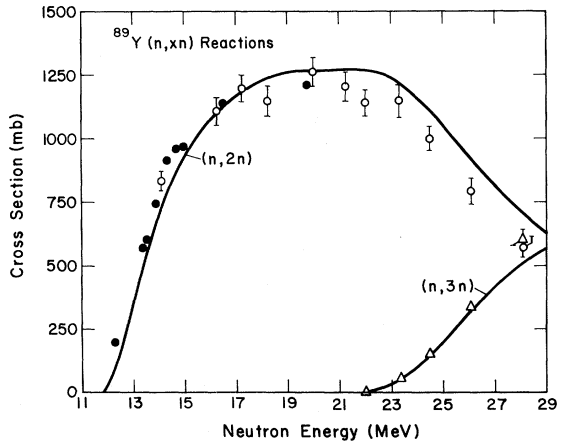

FIG. 4. Excitation functions for $^{89}Y(n, xn)$ reactions. Experimental values for $(n, 2n)$ (○), and $(n, 3n)$ (△). Also shown are earlier measurements of Ref. 14 (●), normalized to the 14.1 MeV value of this work. The lines are calculated values.

TABLE V. $^{89}Y(n,xn)$ cross sections.

$\bar{E}_n$ (MeV)	$\Delta\bar{E}_n$ (MeV)	$^{89}Y(n,2n)^{88}Y$ σ(mb)	$^{89}Y(n,3n)^{87}Y$ σ(mb)
14.10	0.05	834± 36	
16.22	0.10	1104± 48	
16.22	0.10	1113± 48	
17.24	0.17	1198± 51	
18.24	0.09	1147± 58	
20.00	0.10	1265± 54	
21.27	0.17	1206± 61	
22.03	0.12	1141± 49	≤5
23.34	0.13	1150± 68	53± 3
24.50	0.12	1004± 43	150± 7
26.07	0.12	793± 47	337± 14
28.06	0.13	571± 39	606± 26
Product $T_{1/2}$		106.6 day	80.0 h
Threshold		11.60 MeV	21.08 MeV

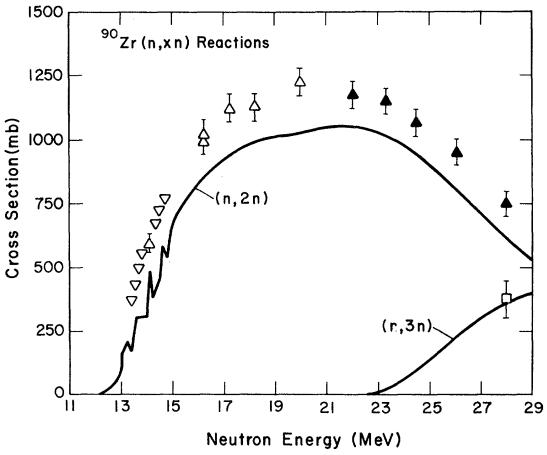

FIG. 5. Excitation functions for $^{90}Zr(n,xn)$ reactions. Cross sections for $(n,2n)$ are shown by (△), $(n,3n)$ by (□). Filled points indicate that the data has been corrected for estimated $^{91}Zr(n,3n)$ reactions. Values from Ref. 14, (▽), were normalized at 14.1 MeV. The lines are the result of calculations described in the text.

particle momentum, $\sigma_{inv}(E_\beta)$ is the inverse cross section of the reaction, and $\rho(U-E_\beta-B_\beta)$ is the level density of the residual nucleus after the emission of a particle having kinetic energy E and binding energy B from an initial compound level of excitation energy U. Crucial to the calculations are the choice of inverse cross sections and level densities.

The particle inverse cross sections were from optical model calculations. For most of the cases studied neutron emission is the major mode of decay; therefore, the comparison with the experimental data is quite dependent upon the choice of neutron inverse cross sections. For neutron energies greater than 3 MeV the tabulation of Mani, Melkanoff, and Iori[28] was used for both reaction formation and inverse cross sections. For lower neutron energies, the cross sections were estimated by other methods and normalized to the values of Mani *et al.* at 3 MeV, since the energy-dependent absorptive part of the potential in Ref. 28 was inadequate at low energies. For $A<180$, the cross sections were calculated by

$$\sigma(e)=\sum_l (2_l+1)\pi\lambda\!\!\!^{-2}T_l(e) \qquad (4)$$

with the transmission coefficients $T_l(e)$ determined from the general relationships presented by Blatt and Weisskopf.[4] For $A>180$ the neutron cross sections were determined using the optical model parameters presented by Auerbach and Moore[29]

TABLE VI. $Zr(n,xn)$ cross sections.

$\bar{E}_n$ (MeV)	$\Delta\bar{E}_n$ (MeV)	$^{Nat}Zr(n,xn)^{89}Zr$ σ(mb)	$^{90}Zr(n,2n)^{89}Zr$ [a] σ(mb)	$^{90}Zr(n,3n)^{88}Zr$ σ(mb)
14.10	0.05		590± 25	
16.23	0.10	524± 22	1018± 44	
16.23	0.10	511± 21	994± 42	
17.24	0.17	576± 24	1119± 47	
18.24	0.09	579± 24	1125± 48	
19.98	0.10	630± 27	1225± 52	
22.02	0.13	604± 26	(1174)	
23.33	0.13	614± 26	(1150)	
24.49	0.12	595± 25	(1070)	
26.06	0.12	534± 23	(950)	
27.99	0.19	446± 19	(750)	374± 71
28.20	0.05	434± 18		
Product $T_{1/2}$		78.4 h		82.56 day
Threshold		12.12 MeV		21.53 MeV

[a] Values in parentheses have been corrected for $^{91}Zr(n,3n)^{89}Zr$.

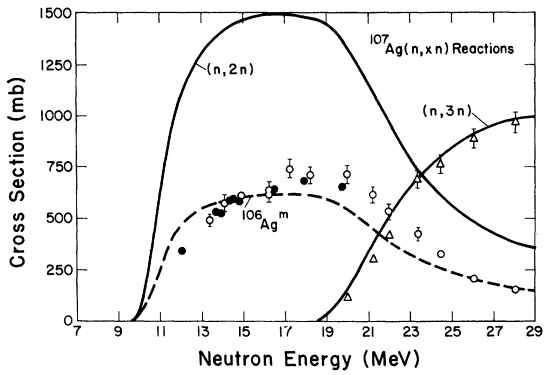

FIG. 6. Excitation functions for ^{107}Ag(n, xn) reactions. Experimental cross sections for ^{107}Ag$(n, 2n)^{106}$Ag^m (○), and $(n, 3n)$ (△). The lines are calculated values. The dashed line (cross section for the isomeric state) is to be compared with the experimental $(n, 2n)$ data. Also shown are normalized values (●) from the relative measurements of Ref. 14.

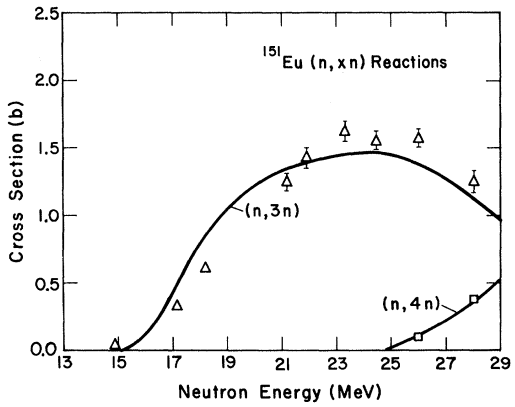

FIG. 7. Excitation functions for ^{151}Eu(n, xn) reactions. Experimental cross sections for $(n, 3n)$ (△), and $(n, 4n)$ (□), and calculated curves.

from their analysis of low energy neutron scattering in this mass region.

The model also allows nuclear deexcitation by proton- and α-particle emission and by γ-ray decay. The inverse cross sections for proton emission were also from tabulations by Mani *et al.*,[28] while those for α emission were calculated using the parabolic barrier approximation presented by Huizenga and Igo.[30]

The γ-ray decay width was determined from the photoabsorption cross section, which was assumed to have a Lorentzian shape centered about the giant dipole resonance:

$$\Gamma_\gamma = \frac{K}{\rho(U)} \int_0^U \frac{E_\gamma^2 \sigma_i \Gamma_i^2}{(E_\gamma^2 - E_i^2)^2 + \Gamma_i^2 E_\gamma^2} \times E_\gamma^2 \rho(U - E_\gamma) dE_\gamma \ . \quad (5)$$

For deformed nuclei the photoabsorption cross section splits into an upper and lower Lorentzian curve. The photoabsorption cross section parameters for the giant dipole resonance, intensity σ_i, width Γ_i, and energy E_i, were taken from simple analytic representations of the tabulated data of Fuller *et al.*[31] The normalization constant K was determined by fitting (n, γ) cross section data for

TABLE VII. ^{107}Ag(n, xn) cross sections.

$\bar{E}_n$ (MeV)	$\Delta \bar{E}_n$ (MeV)	^{107}Ag$(n, 2n)^{106}$Ag^m σ(mb)	^{107}Ag$(n, 3n)^{105}$Ag σ(mb)
13.41	0.05	495 ± 25	
14.10	0.05	573 ± 29	
14.92	0.05	610 ± 30	
16.23	0.09	637 ± 31	
16.23	0.10	629 ± 31	
17.23	0.17	741 ± 37	
18.23	0.10	716 ± 35	5^{+8}_{-5}
19.98	0.11	715 ± 35	117 ± 16
21.25	0.18	618 ± 30	300 ± 15
22.00	0.14	534 ± 26	420 ± 20
23.36	0.11	423 ± 21	691 ± 35
24.48	0.13	323 ± 16	767 ± 39
26.06	0.13	210 ± 10	898 ± 45
28.05	0.14	157 ± 8	969 ± 49
Product $T_{1/2}$		8.27 day	40.75 day
Threshold		9.64 MeV	17.64 MeV

TABLE VIII. ^{151}Eu(n,xn) cross sections.

$\bar{E}_n$ (MeV)	$\Delta\bar{E}_n$ (MeV)	^{151}Eu$(n,3n)^{149}$Eu σ(mb)	^{151}Eu$(n,4n)^{148}$Eu σ(mb)
14.85	0.05	15± 7	
17.18	0.19	334± 14	
18.17	0.14	606± 27	
21.18	0.23	1241± 52	
21.92	0.21	1424± 62	
23.31	0.15	1615± 70	
24.45	0.16	1558± 76	
26.01	0.16	1570± 93	105± 5
28.00	0.18	1250±107	390±20
Product $T_{1/2}$		97.3 day	54.2 day
Threshold		14.51 MeV	22.77 MeV

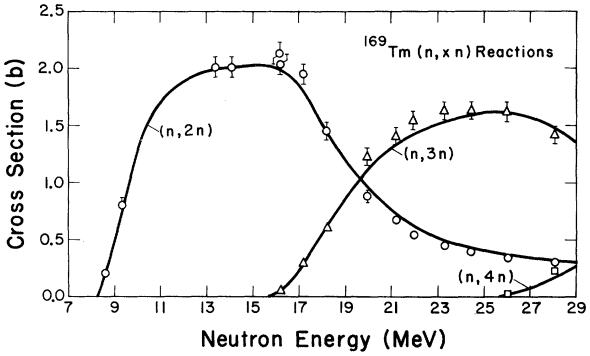

FIG. 8. Excitation functions for ^{169}Tm(n,xn) reactions. Experimental cross sections for $(n,2n)$ (○), $(n,3n)$ (△), and $(n,4n)$ (□). The lines are calculated values.

^{169}Tm.

The level densities were calculated by the method developed by Moretto.[32] This is a single-particle-based level density formalism which directly includes pairing effects as determined from solution of the BCS equations. The Moretto model also evaluates the "spin cut-off parameter" σ as a function of the nuclear excitation energy. The compound nuclear spin distribution can then be estimated by

$$P(J) = (2J+1)\exp[-(J+1/2)^2/2\sigma^2] \ . \qquad (6)$$

The single-particle levels used for the level density analysis were generated with the Nilsson potential using parameters from Ragnarsson.[33] Reaction Q values were from Wapstra and Gove.[34]

For neutron emission in which the decay was to levels below 2-MeV excitation energy, the level densities were transformed from a continuous distribution to a synthetic discrete set of low-lying levels. The energy of the ith level was calculated to be

$$E_i = E_{i-1} + 1/\bar{\rho}(E_i) \ , \qquad (7)$$

where $\bar{\rho}(E_i)$ is the average level density in the 100-keV interval nearest to E_i. The spin of the level was assigned by random number using the cumulative spin probability distribution:

$$P(J_c) = \frac{\int_0^{J_c+1/2}(2J+1)\exp[-(J+\frac{1}{2})^2/2\sigma^2]\,dJ}{\int_0^{\infty}(2J+1)\exp[-(J+\frac{1}{2})^2/2\sigma^2]\,dJ} \ . \qquad (8)$$

For these low energy neutron decays the rela-

TABLE IX. ^{169}Tm(n,xn) cross sections.

$\bar{E}_n$ (MeV)	$\Delta\bar{E}_n$ (MeV)	^{169}Tm$(n,2n)^{168}$Tm σ(mb)	^{169}Tm$(n,3n)^{167}$Tm σ(mb)	^{169}Tm$(n,4n)^{166}$Tm σ(mb)
8.65	0.24	210± 9		
9.37	0.25	812± 47		
13.43	0.05	2009± 85		
14.10	0.05	2010± 85		
16.21	0.11	2131±105	42± 3	
16.21	0.11	2034± 86	42± 3	
17.20	0.18	1947± 82	292±13	
18.20	0.12	1455± 62	612±26	
19.95	0.13	885± 38	1230±52	
21.22	0.20	680± 29	1405±60	
21.96	0.17	550± 24	1533±65	
23.32	0.14	453± 62	1627±69	
24.47	0.14	404± 27	1621±69	
26.03	0.15	343± 36	1620±68	26± 1
28.02	0.16	303± 35	1424±61	231±10
Product $T_{1/2}$		93.0 day	9.29 day	7.85 h
Threshold		8.11 MeV	14.96 MeV	23.74 MeV

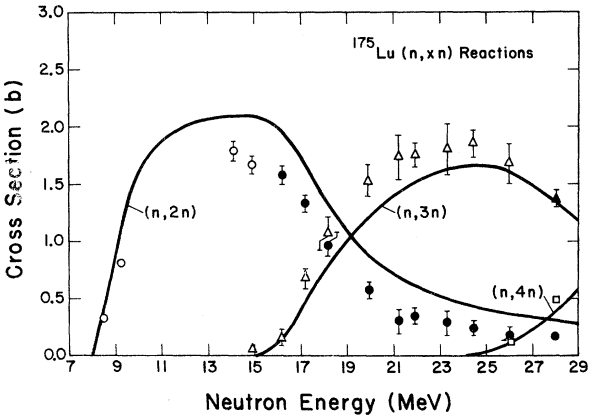

FIG. 9. Excitation functions for ^{175}Lu(n, xn) reactions. Cross sections for $(n, 2n)$ (○), $(n, 3n)$ (△), and $(n, 4n)$ (□), and calculated curves. Filled points indicate that the experimental data has been corrected for estimated ^{176}Lu(n, xn) reactions.

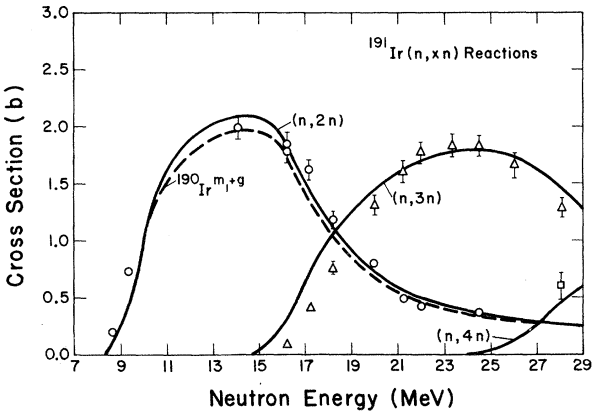

FIG. 10. Excitation functions for ^{191}Ir(n, xn) reactions. Experimental cross sections for ^{191}Ir$(n, 2n)^{190}$Ir$^{m_1+g}$ (○), $(n, 3n)$ (△), and $(n, 4n)$ (□). The lines are the results of calculations described in the text. The dashed line is to be compared with the $(n, 2n)$ data.

tive intensity of the branch decaying to the level at E_i is given by

$$I(U, E_i) = E_n \sigma_{\text{tot}}(E_n) \sum_{J_c} P(J_c) \frac{\sum_{l=|J_c - J_r| - 1/2}^{J_c + J_r} (2l+1) T_l}{\sum_{l=0}^{\infty} (2l+1) T_l}, \quad (9)$$

where E_n is the kinetic energy of the evaporated neutron, $\sigma_{\text{tot}}(E_n)$ is the total compound reaction cross section for an incident neutron of energy E_n, J_c is the spin of the decaying level whose probability is given by a normalization of Eq. (6), J_r is the spin of the residual level at E_i as assigned from Eq. (8), l is the orbital angular momentum of the emitted neutron, and T_l is the transmission coefficient for emission of an l-wave neutron.

Similarly for incident neutron energies below 2 MeV (primarily for n, γ cross sections), the spin population distribution in the compound nucleus was determined by coupling the spin of the target ground state with the partial-wave-weighted trans-

TABLE X. Lu(n, xn) cross sections.

$\bar{E}_n$ (MeV)	$\Delta \bar{E}_n$ (MeV)	$^{\text{Nat}}$Lu$(n, xn)^{174}$Lu σ(mb)	$^{\text{Nat}}$Lu$(n, xn)^{173}$Lu σ(mb)	^{175}Lu$(n, 2n)^{174}$Lu [a] σ(mb)	^{175}Lu$(n, 3n)^{173}$Lu [b] σ(mb)	^{175}Lu$(n, 4n)^{172}$Lu σ(mb)
8.51	0.34	315± 15		323± 15		
9.27	0.36	795± 34		816± 35		
14.10	0.05	1742± 74		1789± 76		
14.92	0.05	1625± 69	54± 29	1668± 71	55± 30	
16.18	0.14	1550± 66	146± 49	(1580)	150± 50	
17.19	0.19	1326± 62	655± 81	(1337)	673± 83	
18.19	0.13	971± 74	1042± 140	(965)	1070± 144	
19.94	0.15	596± 60	1490± 135	(574)	1530± 138	
21.21	0.21	336± 110	1695± 192	(303)	1740± 197	
21.94	0.19	376± 50	1712± 100	(342)	1757± 103	
23.32	0.14	321± 97	1762± 217	(287)	1808± 227	
24.46	0.15	280± 49	1812± 111	(246)	1855± 114	
26.03	0.15	221± 50	1646± 167	(190)	1678± 168	120± 5
28.01	0.17	193± 37	1358± 90	(169)	(1360)	490± 21
Product $T_{1/2}$		142 day (m) 1204 day (g)	512 day			6.7 day
Threshold		7.70 MeV	14.53 MeV			22.76 MeV

[a] Values in parentheses have been corrected for ^{176}Lu$(n, 3n)^{174}$Lu.
[b] Value in parentheses has been corrected for ^{176}Lu$(n, 4n)^{173}$Lu.

TABLE XI. $^{191}Ir(n,xn)$ cross sections.

$\bar{E}_n$ (MeV)	$\Delta\bar{E}_n$ (MeV)	$^{191}Ir(n,2n)^{190}Ir^{m_1+g}$ σ(mb)	$^{191}Ir(n,3n)^{189}Ir$ σ(mb)	$^{191}Ir(n,4n)^{188}Ir$ σ(mb)
8.64	0.26	187± 9		
9.34	0.28	723± 36		
14.10	0.05	1995±100		
16.20	0.12	1785± 89	85± 5	
16.21	0.12	1843± 92	92± 5	
17.22	0.18	1625± 85	403±23	
18.22	0.11	1183± 59	748±43	
19.97	0.12	793± 40	1303±76	
21.24	0.19	496± 29	1602±80	
21.98	0.15	425± 25	1771±89	
23.35	0.12		1834±91	
24.48	0.13	367± 25	1832±91	
26.05	0.13		1662±97	
28.03	0.15		1282±75	610±121
Product $T_{1/2}$		(11.78±0.10) day	(13.10±0.10) day	41.5 h
Threshold		8.16 MeV	14.44 MeV	22.74 MeV

mission coefficients in a manner analogous to Eq. (9).

Except for the two low neutron-energy cases just discussed, the calculations did not explicitly take into account the angular momentum throughout the course of the reaction. Since the angular momentum transfer in neutron reactions is relatively modest, the effects are adequately averaged for the calculation of total reaction cross sections. No sum was made over the l values for entrance and exit channels and the reaction and inverse cross sections were the total compound nonelastic values.

The preequilibrium deexcitation component was calculated using the formalism of Blann and Mignerey,[35] which estimates the particle emission from the nucleus as it changes from the one particle-no hole initial interaction condition to the many particle-many hole configuration of the compound state. Significant quantities entering into the calculations are: (1) The ratio of the available phase space between the residual and excited nucleus, calculated using the particle-hole state densities given by Ericson[36]; and (2) the probability that an excited particle will decay into the continuum before it excites another particle-hole state. The transition rate for emission into the continuum is the product of the penetrability rates and continuum state densities. The particle-energy-dependent equation for the rate of

TABLE XII. $^{193}Ir(n,xn)$ cross sections.

$\bar{E}_n$ (MeV)	$\Delta\bar{E}_n$ (MeV)	$^{193}Ir(n,n')^{193}Ir^{m}$ σ(mb)	$^{193}Ir(n,2n)^{192}Ir^{m_1+g}$ σ(mb)
7.57	0.25	1830±114	
8.59	0.26	1200±125	
8.61	0.26		426± 21
9.34	0.28	548±271	1070± 55
14.10	0.05		2005±100
14.70	0.24	248± 21	
16.20	0.12		1780± 88
16.21	0.12		1843± 93
17.22	0.18		1550± 80
18.22	0.11		1040± 59
19.97	0.12		560± 34
21.24	0.19		508± 34
Product $T_{1/2}$		(10.60±0.11) day	74.2 day
Threshold		0.08 MeV	7.81 MeV

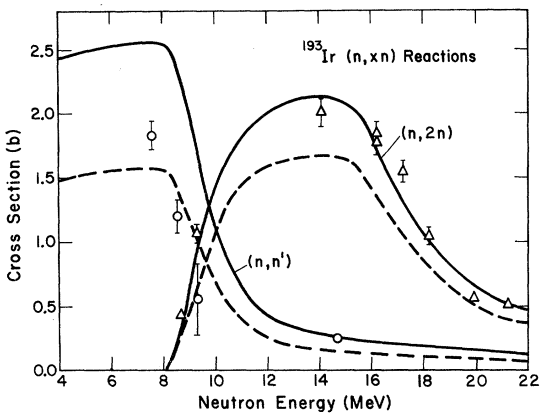

FIG. 11. Calculated and experimental cross sections for ^{193}Ir(n, xn) reactions. Experimental cross sections for ^{193}Ir$(n, n')^{193}$Ir^m (○), and ^{193}Ir$(n, 2n)^{192}$Ir$^{m_1+g}$ (△), and calculated total (solid curves) and isomeric level (dashed curves) cross sections. The data is to be compared with the dashed curves.

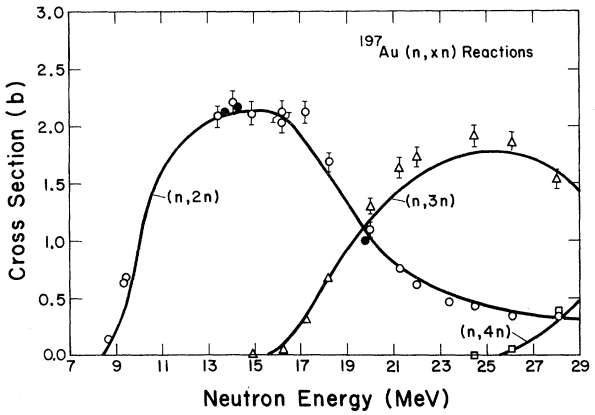

FIG. 12. Excitation functions for ^{197}Au(n, xn) reactions. Experimental cross sections for $(n, 2n)$ (○), $(n, 3n)$ (△), and $(n, 4n)$ (□), and calculated curves. Also shown are earlier measurements (Ref. 14) normalized to the 13.4 MeV value of this work (●).

internal transition λ_{n+2} was quantitatively evaluated in Ref. 35 by fitting the average mean free paths of excited nucleons in nuclear matter as calculated by Kikuchi and Kawai.[37] Blann and Mignerey also included a scaling factor k in their expression [i.e., $\lambda_{n+2} = f(E)/k$] to permit longer mean free paths, which can occur from scattering restrictions (imposed by angular momentum coupling effects and the requirement of discrete energy transitions) that were not included by Kikuchi and Kawai in their treatment of free nucleon-nucleon scattering data. In this work, a value of $k = 4$ reproduced the experimental data for the ^{169}Tm-$(n, 2n)^{168}$Tm cross section adequately (see Fig. 1) and was used in all computations. A value of $k = 1$ would correspond to the mean free paths in Kikuchi and Kawai.

Some of the experimental data present cross sections for production of nuclei in isomeric levels. An accurate prediction of these yields would require explicit consideration of the angular momentum effects from the l-wave transfer in the

TABLE XIII. ^{197}Au(n, xn) cross sections.

$\bar{E}_n$ (MeV)	$\Delta\bar{E}_n$ (MeV)	^{197}Au$(n, 2n)^{196}$Au σ(mb)	^{197}Au$(n, 3n)^{195}$Au σ(mb)	^{197}Au$(n, 4n)^{194}$Au σ(mb)
8.65	0.23	147± 7		
9.32	0.31	629± 31		
9.38	0.24	680± 34		
13.41	0.05	2097± 89		
14.10	0.05	2213± 94		
14.89	0.05	2116± 89		
16.19	0.13	2046± 87	35± 20	
16.20	0.12	2130± 90		
17.23	0.17	2125± 90	309± 15	
18.23	0.10	1691± 72	670± 32	
19.98	0.11	1096± 47	1296± 59	
21.25	0.18	750± 38	1637± 78	
22.00	0.14	613± 31	1734± 79	
23.36	0.12	469± 28		
24.48	0.13	427± 21	1916± 95	2^{+3}_{-2}
26.06	0.13	340± 18	1859± 93	57± 3
28.08	0.14	339± 17	1535± 71	370± 21
Product $T_{1/2}$		6.18 day	183 day	1.625 day
Threshold		8.12 MeV	14.82 MeV	23.27 MeV

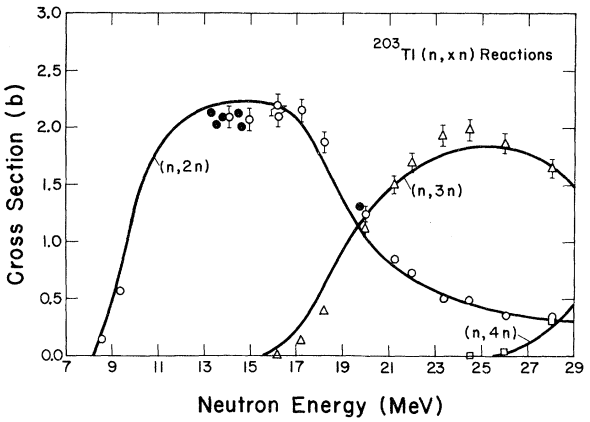

FIG. 13. Excitation functions for ^{203}Tl(n, xn) reactions. Experimental cross sections for $(n, 2n)$ (○), $(n, 3n)$ (△), and $(n, 4n)$ (□). Filled points are earlier measurements (Ref. 14) normalized to the 14.1 MeV value of this work. The lines are the calculated values.

initial reaction through the particle evaporation and γ-ray cascade. Since such detailed angular momentum effects were not included in the model, only a simple estimate of the isomeric population was made by assuming the yield is proportional to the angular momentum states available in the residual nucleus:

$$\sigma_{(n,xn_i)} = \sigma_{(n,xn)} \frac{\int_{(J_i+J_g)/2}^{\infty} (2J+1)\exp[-(J+\frac{1}{2})^2/2\sigma^2]dJ}{\int_0^{\infty} (2J+1)\exp[-(J+\frac{1}{2})^2/2\sigma^2]\,dJ} \quad (10)$$

where $\sigma_{(n,xn)}$ is the total production cross section, $\sigma_{(n,xn_i)}$ is the cross section for the isomer, J_i is the spin of isomer; $J_i > J_g$, J_g is the spin of ground state. A value of 3 has been used for the "spin cut-off parameter" σ for nuclei with Z less than 50, and 4 for the remaining ones.[38]

VI. DISCUSSION AND COMPARISON OF CALCULATED AND OBSERVED CROSS SECTIONS

The artificial method of generating low-lying levels gives a capability for determining average properties of discrete levels where complete spectroscopic data are not available, and should give a better estimate of the transition strength than using a continuous representation. In general, there is good agreement for the total cross sections for neutron-induced reactions. There is, however, evidence that at low residual excitation energies the inverse neutron cross sections are not adequate for some cases, specifically near the thresholds (see Figs. 1–13). For any individual isotope the calculations could be improved by adjusting the parameters. Since we have chosen not to do so, we are reasonably confident that calculations for other nuclei would agree with experimental values to an accuracy comparable with those presented here.

The effect of the preequilibrium component is substantial (see Fig. 1). Clearly an adequate representation of the experimental $(n, 2n)$ data at the higher neutron energies could not be obtained without this contribution.

(1) ^{45}Sc. The experimental data are for the 2.44-d

TABLE XIV. Tl(n,xn) cross sections.

$\bar{E}_n$ (MeV)	$\Delta\bar{E}_n$ (MeV)	^{203}Tl$(n, 2n)^{202}$Tl σ(mb)	^{203}Tl$(n, 3n)^{201}$Tl σ(mb)	^{203}Tl$(n, 4n)^{200}$Tl σ(mb)	^{205}Tl$(n, 4n)^{202}$Tl σ(mb)
8.61	0.25	158± 7			
9.32	0.31	576±24			
9.36	0.26	569±24			
14.10	0.05	2090±89			
14.89	0.05	2077±88			
15.00	0.05		≤10± 6		
16.20	0.12	2103±89	18± 6		
16.20	0.12	2196±93			
17.23	0.17	2150±92	136± 6		
18.23	0.10	1865±80	386±17		
19.99	0.11	1243±53	1117±48		
21.25	0.18	851±36	1499±64		
22.01	0.14	728±31	1692±72		
23.35	0.12	508±21	1930±82		7^{+10}_{-7}
24.49	0.13	490±21	1980±87	1^{+7}_{-1}	9± 6
26.06	0.12	362±15	1858±79	39±11	137± 8
28.05	0.14	330±14	1644±70	304±14	546±23
Product $T_{1/2}$		12.5 day	3.046 day	26.1 h	
Threshold		7.76 MeV	14.72 MeV	23.03 MeV	22.02 MeV

6+ isomeric level which is estimated [from Eq. (10)] to be 0.329 of the total $(n, 2n)$ cross section. See Fig. 2 and Table III. The agreement between the experimental and calculated values is satisfactory. Earlier data of Prestwood and Bayhurst[14] for the total $(n, 2n)$ cross section (which has been recalculated using better absolute counting efficiencies) indicate that the computations may overestimate the cross section at higher neutron energies.

(2) ^{58}Ni. The agreement between measured and calculated cross sections for this isotope is the poorest of the cases studied. The computation overestimates the cross section for the $(n, 2n)$ reaction by a factor of 2 (Fig. 3 and Table IV). Contrary to the suppositions in the model, in this case the neutron-out processes are a minor part of the total nonelastic cross section of 1300 mb. The majority is in the proton-out channels and uncertainties in optical model proton inverse cross sections may account for the large deviation. Since the specific properties of the fine structure in Fig. 3 are due to decay channel competition obtained using artificially generated low-lying single-particle levels, a direct correspondence between the calculations and data is not expected. Such pronounced structure would be possible in nuclei that are expected to have decreased level densities at low excitation energies due to their proximity to major nuclear shells. The structure is shown merely to indicate the magnitude of possible deviations from a smooth curve.

(3) ^{89}Y. Experimental and calculated results for the $(n, 2n)$ and $(n, 3n)$ reactions are shown in Fig. 4 and Table V. Although there is reasonable agreement at the peak of the $(n, 2n)$ cross section, there are deviations near threshold and in the tailing region. Since ^{89}Y is a closed neutron shell nucleus, there are relatively few low-lying levels for decay channels, which may result in discrepancies in the calculated values. In addition, the (n, np) threshold is at 7.15 MeV, 4.45 MeV below the $(n, 2n)$ threshold. Even though the proton channel is inhibited by the Coulomb barrier, the computation of proton- and γ-decay widths for such a demanding test as this nuclide may not be entirely adequate. The $(n, 3n)$ excitation function appears to be well represented near threshold, but begins to deviate near 28 MeV.

(4) ^{90}Zr. Table VI contains the production cross sections for 78.4-h ^{89}Zr from zirconium of natural isotopic composition. The total ^{90}Zr$(n, 2n)$ cross sections derived from these data lack the 6% branch of the 4.18-min isomer which does not decay to the ground state. Above 21 MeV, the ^{90}Zr$(n, 2n)$ cross sections shown in parentheses have been corrected for ^{91}Zr$(n, 3n)^{89}$Zr using cross sections from the model calculations.

The agreement between experimental and computed $(n, 2n)$ cross sections for ^{90}Zr is less satisfactory than for ^{89}Y (see Fig. 5). For many nuclear studies ^{90}Zr can be considered a doubly closed shell nucleus, since the 40th proton fills the $2p_{1/2}$ level and the 50th neutron closes the $1g_{9/2}$ level. The threshold for (n, np) is 3.66 MeV below the $(n, 2n)$ threshold.

(5) ^{107}Ag. Experimental data for the spin-6 8.4-d isomer of ^{106}Ag, which is estimated to have 0.417 of the total $(n, 2n)$ cross section, are shown in Table VII and Fig. 6. The computed values agree with the data in the 13–16 MeV region but are too high nearer threshold and too low between 17 and 25 MeV. Such differences are certainly possible from the inadequacies of the simple method used to estimate isomeric yields. Except near threshold the agreement between experimental and computed $(n, 3n)$ cross sections is good.

(6) ^{151}Eu. Figure 7 compares experimental data (Table VIII) and computed cross sections for the $(n, 3n)$ and $(n, 4n)$ reactions. Again the agreement is satisfactory except near the $(n, 3n)$ threshold.

(7) ^{169}Tm. Cross sections for the $(n, 2n)$ and (n, γ) reactions for this nuclide were used to determine the two scaling factors in the computations (Fig. 8 and Table IX). The curves for the $(n, 3n)$ and $(n, 4n)$ cross sections reproduce the experimental data satisfactorily.

(8) ^{175}Lu. The large errors on the experimental data in Fig. 9 reflect poor counting statistics and the uncertainty from large subtractions of natural ^{176}Lu and/or (n, γ) activities. The γ activity from ^{174}Lu originates from two isomers which were not resolved by decay except for the 14.1-MeV irradiation. Other total $(n, 2n)$ cross sections were calculated using the experimental isomer ratio determined at 14.1 MeV, $\sigma(n, 2n_m)/\sigma(n, 2n_g) = 0.475$. Table X lists the production cross sections for ^{174}Lu and ^{173}Lu from normal Lu. These data have been transformed into $(n, 2n)$ and $(n, 3n)$ cross sections for ^{175}Lu, respectively, by subtracting the model-calculated production of these isotopes by $(n, 3n)$ and $(n, 4n)$ reactions on ^{176}Lu (a 2.6% abundant isotope) when it was necessary (shown in parentheses). The deviations between excitation function and experimental data is larger than expected for this case, especially since charged-particle emission from such a heavy nucleus is inhibited. For these reactions experimental errors are known to be larger due to the nature of the radiations and half-lives involved, decay scheme knowledge, the presence of ^{176}Lu natural radioactivity, and our inability to resolve $^{174}Lu^{m,g}$ at these activity levels. Thus, for this case the deviations may be due to experimental difficulties

rather than model deficiencies.

(9) ^{191}Ir. Values for the $(n, 2n)$, $(n, 3n)$, and $(n, 4n)$ cross sections (Table XI) and the computed excitation functions are shown in Fig. 10. The experimental $(n, 2n)$ cross sections lack 94% of the yield of the spin-11 3.1-h m_2 isomeric state of ^{190}Ir which decays by electron capture, an estimated 0.056 of the total value. The curves represent the data satisfactorily except near the thresholds of the three reactions.

(10) ^{193}Ir. The data for this nuclide are in Table XII. For both the (n, n') and $(n, 2n)$ reactions only isomeric yields were measured. The 10.6-day spin-$\frac{11}{2}$ isomer of ^{193}Ir is estimated to have 0.61 of the total (n, n') cross section; the agreement between the curve and the data is only moderate even considering the large experimental uncertainties (Fig. 11). For the $(n, 2n)$ reaction, the yield of the 241-yr spin-9 isomer which was not measured is estimated to be 0.22 of the total cross section. The experimental results for the 74.2-day ground state are much closer to the total value, suggesting that there are other high spin decay channels which feed the ground state directly.

(11) ^{197}Au. The computed cross sections for gold (Fig. 12) are in reasonable agreement with the experimental data (Table XIII).

(12) ^{203}Tl. The largest discrepancies between data and the calculations are near the threshold for the $(n, 3n)$ reaction, where the experimental cross sections rise more slowly (Fig. 13). The calculations also agree with the three experimental points for ^{205}Tl$(n, 4n)^{202}$Tl satisfactorily (not shown); see Table XIV.

ACKNOWLEDGMENTS

The authors are grateful to Dr. Donald W. Barr for his helpful discussions and interest, Dr. G. F. Grisham for her calibration and aid with the rare earth samples, John C. Martin and Louis J. Morrison for their technical assistance, and the operating personnel at the Los Alamos Cockcroft-Walton and Van de Graaff accelerators, all of this laboratory.

We would like to thank Professor L. G. Moretto for his help in providing the single-particle based level density code and Professor M. Blann for providing the preequilibrium decay code.

[1]D. W. Barr, C. I. Browne, and J. S. Gilmore, Phys. Rev. 123, 859 (1961).
[2]S. Pearlstein, Nucl. Sci. Eng. 23, 238 (1965).
[3]H. Büttner, A. Linder, and H. Meldner, Nucl. Phys. 63, 615 (1965).
[4]J. M. Blatt and V. F. Weisskopf, *Theoretical Nuclear Physics* (Wiley, New York, 1952), pp. 311–379.
[5]H. Liskien, Nucl. Phys. A118, 379 (1968).
[6]J. J. Griffin, Phys. Rev. Lett. 17, 478 (1966).
[7]M. Blann, Phys. Rev. Lett. 21, 1357 (1968).
[8]F. C. Williams, Jr., Phys. Lett. 31B, 184 (1970).
[9]G. D. Harp and J. M. Miller, Phys. Rev. C 3, 1847 (1971).
[10]M. Blann and F. M. Lanzafame, Nucl. Phys. A142, 559 (1970).
[11]R. L. Henkel, J. E. Perry, and R. K. Smith, Phys. Rev. 99, 1050 (1955).
[12]L. Cranberg, A. H. Armstrong, and R. L. Henkel, Phys. Rev. 104, 1639 (1956).
[13]E. A. Kuzmin, A. A. Ogloblin, N. I. Sidorov, A. R. Faiziev, and G. B. Yankov, in Proceedings of the Symposium on Applications of Nuclear Data in Science and Technology, Paris, 1973 (unpublished), IAEA/SM-170/22.
[14]R. J. Prestwood and B. P. Bayhurst, Phys. Rev. 121, 1438 (1961).
[15]J. W. Barnes, B. P. Bayhurst, B. H. Erkkila, J. S. Gilmore, N. Jarmie, and R. J. Prestwood, J. Inorg. Nucl. Chem. 37, 399 (1975).
[16]B. P. Bayhurst and R. J. Prestwood, J. Inorg. Nucl. Chem. 23, 173 (1961).
[17]Los Alamos Report No. LA-1721, 1958, edited by J. Kleinberg (unpublished), 2nd ed.
[18]B. J. Snyder, Nucl. Instrum. Methods 53, 313 (1967).
[19]*Nuclear Data Sheets*, compiled by K. Way *et al.* (Printing and Publishing Office, National Academy of Sciences-National Research Council, Washington, D.C.), NRC 5-5-133.
[20]C. Lederer, J. Hollander, and I. Perlman, *Table of Isotopes* (Wiley, New York, 1967).
[21]G. A. Brinkman, A. H. W. Aten, Jr., and J. Th. Veenboer, Int. J. Appl. Radiat. Isot. 14, 153 (1963).
[22]N. Jarmie and B. H. Erkkila, Bull. Am. Phys. Soc. 17, 902 (1972).
[23]W. A. Gibson, W. R. Burrus, J. W. Wachter, and C. F. Johnson, Nucl. Instrum. Methods 46, 29 (1967), and references contained therein.
[24]J. C. Hopkins and G. Breit, Nucl. Data A9, 1937 (1971).
[25]P. Jessen, M. Bormann, F. Dreyer, and H. Neuert, Nucl. Data A1, 103 (1966).
[26]A. Fabry, M. deCoster, G. Minsart, J. C. Schepers, and P. Vandeplas, in Proceedings of the Second IAEA Conference on Nuclear Data for Reactors, Helsinki, Finland, 1970 (unpublished), Vol. 2, p. 535.
[27]C. F. Williamson, J.-P. Boujot, and J. Picard, Tables of Range and Stopping Power of Chemical Elements For Charged Particles of Energy 0.5 to 500 MeV [Centre d'Eluotes Nucleaires de Saclay, Saclay Rapport No. CEA-R3042, 1966 (unpublished)].
[28]G. S. Mani, M. A. Melkanoff, and I. Iori, Centre d'Etudes Nucleaires de Saclay Rapports Nos. CEA-2379, 2380 (1963).
[29]E. H. Auerbach and S. O. Moore, Phys. Rev. 135, B895 (1964).

[30]J. R. Huizenga and G. Igo, Nucl. Phys. 29, 462 (1962).
[31]E. G. Fuller, H. M. Gerstenberg, H. Vander Molen, and T. C. Dunn, Photonuclear Reaction Data, 1973 [National Bureau of Standards Special Publication No. 380, 1973 (unpublished)].
[32]L. G. Moretto, Nucl. Phys. A182, 641 (1972); A185, 145 (1972).
[33]I. Ragnarsson, in Proceedings of the International Conference on Properties of Nuclei Far from the Region of Beta Stability, Leysin, Switzerland, 1970 [CERN Report No. 70-30, 1970 (unpublished)], Vol. II, p. 847.
[34]A. H. Wapstra and N. B. Gove, Nucl. Data A9, 265 (1971).
[35]M. Blann and A. Mignerey, Nucl. Phys. A186, 245 (1972).
[36]T. Ericson, Adv. Phys. 9, 425 (1960).
[37]K. Kikuchi and M. Kawai, *Nuclear Matter and Nuclear Reactions* (North-Holland, Amsterdam, 1968).
[38]J. R. Huizenga and R. Vandenbosch, Phys. Rev. 120, 1305 (1960); R. Vandenbosch and J. R. Huizenga, *ibid.* 1313 (1960).